Journal of Systems Engineering and Electronics
Vol. 31, No. 5, October 2020, pp.871 – 883

Design, analysis and optimization of random access inter-satellite ranging system

XU Xiaoyi, WANG Chunhui*, and JIN Zhonghe

Micro-Satellite Research Center, Zhejiang University, Hangzhou 310027, China

Abstract: In this paper, a random access inter-satellite ranging (RAISR) system is designed. The ranging accuracy is optimized by an algorithm to greatly improve the ranging accuracy. This paper verifies the feasibility of the RAISR system through a series of theoretical analysis, numerical simulation, hardware system design and testing. The research work brings the solution to the design and accuracy optimization problem of the RAISR system, which eliminates the main error caused by the satellite dynamic characteristics and frequency source drift of the RAISR system. The accuracy of the measurement system has been significantly improved.

Keywords: satellite ranging, random access, distributed network.

DOI: 10.23919/JSEE.2020.000067

1. Introduction

Since the beginning of the 21st century, the application results of satellite communication measurement technology have brought about major changes in communication, navigation and positioning, etc., but a single spacecraft has been unable to meet the requirements of low cost, high reliability, fastness and efficiency for modern aerospace technology. In order to adapt to a variety of new user needs, distributed satellite systems came into being [1]. With the concepts of distributed satellite systems such as formation flying, separation module spacecraft, and constellation, the cooperation of multiple satellites and space missions has become an important trend in space technology development [2 – 4]. Most of the satellite systems that have been in-orbit experiments are networks of multiple homogeneous satellites [5,6], such as the National Aeronautics and Space Administration (NASA) Edison Demonstration of Smallsat Networks (EDSN) Project [7,8], the Swift Gamma-Ray Burst Mission Project [9], the European Space Agency (ESA) Project for On-board Autonomy (PROBA-3) [10], and the Chinese Academy of Sciences Space Ultra-Low Frequency Radio Observatory (SULFRO) Project [11]. In order to extend the capabilities of individual systems and further reduce development costs, the concept of heterogeneous networks was proposed and applied to satellite networks, including federated satellite systems (FSS) proposed by Selva et al. [12], the heterogeneous spacecraft network (HSN) [13] proposed by Faber et al., and the Internet of Satellites (IoS) proposed by Ruiz et al. [14]. These systems have different mission objectives. Satellites from different research institutes can communicate with each other, and integrate heterogeneous networks to share functions such as shared payload data, forwarding remote command and telemetry data, and on-board hardware resource. Alessandro [15] pointed out that heterogeneous networks would become one of the three major development trends of distributed satellite systems in the future. At present, many research institutions and scholars have proposed to adopt a random peer-to-peer network architecture [16 – 29]. Due to the randomness and irregularity of satellite distribution in heterogeneous networks [30], regular and orderly formation flying in homogeneous networks is no longer suitable for heterogeneous networks, so random networking has become an area we need to focus on. For stochastic networking technology, inter-satellite relative measurement is the premise to ensure the coordinated implementation of space system tasks. Inter-satellite communication measurements can reduce the dependence on ground stations, such as distributed satellite systems, small satellite formation flying, and satellite communication systems, reduce signal transmission delays, and improve the invulnerability and maneuverability of the entire system. Thus the satellite needs to have the capability of inter-satellite ranging.

Cooperative network refers to a network where both anchor nodes and other nodes need to communicate with the located node [31]. The location of anchor nodes generally depends on global poisoning system (GPS). GPS costs are

Manuscript received November 18, 2019.

*Corresponding author.

This work was supported by the National Natural Science Foundation of China (61525403).

relatively high, and it may be unavailable in some cases. It becomes very important for the topological relationship between nodes to realize the co-location between nodes. The scheme proposed in this paper can be applied to responsive dynamic wireless sensor networks (WSNs), that is, data information is transmitted only when a specific situation occurs in the network. Each node independently completes the positioning process through ranging information and is not limited to GPS [32 – 35].

According to the characteristics and requirements of inter-satellite communication and ranging of distributed satellite systems, this paper designs a random access inter-satellite ranging (RAISR) system scheme, and eliminates the main error through the precision optimization approach, which greatly optimizes the ranging accuracy. This is very important for the future collaborative space mission, filling the gap in the RAISR system. This paper studies the ultra high frequency (UHF) band, but the scheme is applicable to communication satellites in each band.

The remainder of this paper is organized as follows. The RAISR system design scheme and the capture method are presented in Section 2. Section 3 includes system ranging accuracy optimization and simulation. Experimental testing and verification are introduced in Section 4. This paper is concluded in Section 5.

2. Scheme of RAISR system

2.1 RAISR ranging scheme design

The principle of dual one-way ranging is that the two satellites perform the ranging measure each other to transmit measurement signals to the other party for distance measurement, and obtain a pair of distance measurement values with opposite magnitudes and opposite directions. And the two measured values are added to effectively separate the clock influences, thereby obtaining more accurate distance measurements. Under the random access system, each satellite transmits a signal, and other visible satellites can complete a one-way distance measurement with respect to the satellite of the transmitted signal. Taking four satellites as an example, the principle of the RAISR system is shown in Fig. 1 below.

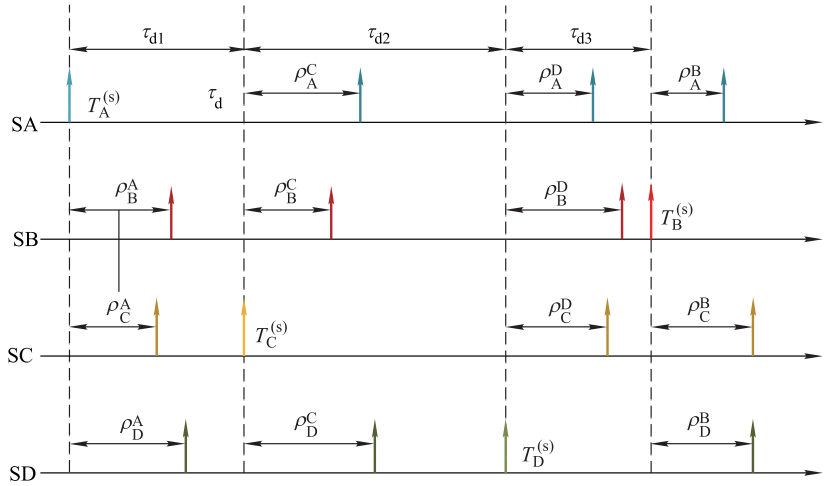

Fig. 1 Four-satellite mutual distance measurement method

Every satellite can transmit signals, and other visible satellites can complete one-way distance measurement with respect to this transmitting signal satellite. Taking four satellites as an example, the multi-satellite mutual ranging method is shown in Fig. 1. The time for each satellite to transmit measurement signals is random. Satellite A (SA), Satellite B (SB), Satellite C (SC), and Satellite D (SD) in the figure send signals at $T_A^{(s)}$, $T_B^{(s)}$, $T_C^{(s)}$ and $T_D^{(s)}$ respectively, $\tau_{d1} = T_C^{(s)} - T_A^{(s)}$, $\tau_{d2} = T_D^{(s)} - T_C^{(s)}$, $\tau_{d3} = T_B^{(s)} - T_D^{(s)}$. When SA emits a signal, the pseudo-ranges of the SA measured by SB, SC, and SD are ρ_A^B, ρ_A^C, and ρ_A^D, respectively. When SC emits a signal, the pseudo-ranges of the SC measured by SA, SB, and SD are ρ_C^A, ρ_C^B and ρ_C^D, respectively. When SD emits a signal, the pseudo-ranges of the SD measured by SA, SB, and SC are ρ_D^A, ρ_D^B and ρ_D^C, respectively. When SB emits a signal, the pseudo-ranges of the SB measured by SA, SC, and SD are ρ_B^A, ρ_B^C and ρ_B^D, respectively. Therefore, each satellite only needs to transmit a signal once, and it can complete the bidirectional distance measurement between any two satellites.

2.2 Error analysis

Under the RAISR system, because there is no strict time synchronization, the measurement accuracy of the dual-one-way system is affected by many factors. After analysis, it is found that the error caused by the dynamic motion of the satellite and the drift of the frequency source is the main systematic error. This section will qualitatively and

quantitatively analyze the main errors of the dual one-way inter-satellite ranging system to obtain measurement system errors.

2.2.1 Satellite dynamic motion error

Fig. 2 shows the effect of dynamic motion on the RAISR system.

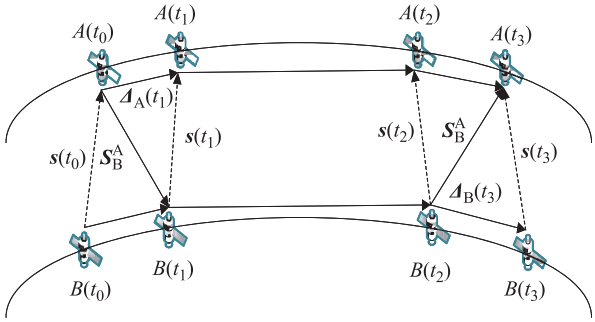

Fig. 2 Effect of satellite dynamic motion on RAISR

$A(t_0)$, $A(t_1)$, $A(t_2)$ and $A(t_3)$ represent SA at time t_0, t_1, t_2 and t_3 respectively. $B(t_0)$, $B(t_1)$, $B(t_2)$ and $B(t_3)$ represent SB at time t_0, t_1, t_2 and t_3 respectively. The distance of the signal propagation within the propagation delay is not equal to the instantaneous distance between SA and SB. The relationship between the signal propagation distance and the instantaneous distance between the satellites is shown in Fig. 2. The nominal time of SA emission time, SB reception time, SB emission time, and SA reception time are respectively recorded as t_0, t_1, t_2 and t_3. $\boldsymbol{S}_{\mathrm{B}}^{\mathrm{A}}$ is the propagation distance vector of the pseudo-code measurement signal indicating SA emission and SB reception, the value of which is equal to $\mathrm{c}\tau_{\mathrm{A}}^{\mathrm{B}}$, where c is the speed of light in vacuum, and $\tau_{\mathrm{A}}^{\mathrm{B}}$ is the transmission time of the signal through the measurement link SA. $\boldsymbol{S}_{\mathrm{A}}^{\mathrm{B}}$ is the propagation distance vector of the pseudo-code measurement signal indicating SB emission and SA reception, the value of which is equal to $\mathrm{c}\tau_{\mathrm{B}}^{\mathrm{A}}$ and $\tau_{\mathrm{B}}^{\mathrm{A}}$ is the transmission time of the signal passing through the measurement link $\boldsymbol{S}_{\mathrm{B}}^{\mathrm{A}}$. $\boldsymbol{\Delta}_{\mathrm{A}}(t_1)$ indicates the distance vector of SA flight during $\tau_{\mathrm{B}}^{\mathrm{A}}$. $\boldsymbol{\Delta}_{\mathrm{B}}(t_3)$ indicates the distance vector of the SB flight during $\tau_{\mathrm{A}}^{\mathrm{B}}$. $\boldsymbol{s}(t_0)$, $\boldsymbol{s}(t_1)$, $\boldsymbol{s}(t_2)$ and $\boldsymbol{s}(t_3)$ respectively represent the inter-satellite distance (ISD) vectors at time t_0, t_1, t_2 and t_3, and the expression of the inter-satellite pseudo-range value is

$$\rho = \frac{\tau_{\mathrm{B}}^{\mathrm{A}} + \tau_{\mathrm{A}}^{\mathrm{B}}}{2} \cdot \mathrm{c} + \frac{[\Delta t_{\mathrm{B}}(t_1) - \Delta t_{\mathrm{A}}(t_0)] - [\Delta t_{\mathrm{B}}(t_2) - \Delta t_{\mathrm{A}}(t_3)]}{2} \cdot \mathrm{c} + \frac{I_{\mathrm{B}}^{\mathrm{A}} + I_{\mathrm{A}}^{\mathrm{B}}}{2} + \frac{d_{\mathrm{B}}^{\mathrm{A}} + d_{\mathrm{A}}^{\mathrm{B}}}{2} + \frac{\varepsilon_{\mathrm{B}}^{\mathrm{A}} + \varepsilon_{\mathrm{A}}^{\mathrm{B}}}{2} \quad (1)$$

where $\Delta t_{\mathrm{B}}(t_1)$ is the difference between the clock face time and the nominal time of SB at t_1, $\Delta t_{\mathrm{A}}(t_0)$ is the difference between the clock face time and the nominal time of SA at t_0, $\Delta t_{\mathrm{B}}(t_2)$ is the difference between the clock face time and the nominal time of SB at t_2, and $\Delta t_{\mathrm{A}}(t_3)$ is the difference between the clock face time and the nominal time of SA at t_3. $I_{\mathrm{B}}^{\mathrm{A}}$ and $I_{\mathrm{A}}^{\mathrm{B}}$ are the distance values respectively corresponding to the ionospheric delay of $S_{\mathrm{B}}^{\mathrm{A}}$ and $S_{\mathrm{A}}^{\mathrm{B}}$. $d_{\mathrm{B}}^{\mathrm{A}}$ and $d_{\mathrm{A}}^{\mathrm{B}}$ are the distance values respectively corresponding to the hardware transmission delay of $S_{\mathrm{B}}^{\mathrm{A}}$ and $S_{\mathrm{A}}^{\mathrm{B}}$. $\varepsilon_{\mathrm{B}}^{\mathrm{A}}$ and $\varepsilon_{\mathrm{A}}^{\mathrm{B}}$ are the distance values respectively corresponding to the measurement noise delay of $S_{\mathrm{B}}^{\mathrm{A}}$ and $S_{\mathrm{A}}^{\mathrm{B}}$.

Temporarily ignoring the influence of other factors such as ionospheric delay and hardware delay, and temporarily thinking that the clock difference remains unchanged, the expression of the inter-satellite pseudo-range value can be expressed as

$$\rho = \frac{r_B^A + r_A^B}{2}. \quad (2)$$

where $r_{\mathrm{B}}^{\mathrm{A}}$ and $r_{\mathrm{A}}^{\mathrm{B}}$ are the propagation distances of the measurement signals in the measurement links $\boldsymbol{S}_{\mathrm{B}}^{\mathrm{A}}$ and $\boldsymbol{S}_{\mathrm{A}}^{\mathrm{B}}$, respectively, and are also the measurement targets of the ranging process.

$$\boldsymbol{s}(t_3) - \boldsymbol{s}(t_2) + \boldsymbol{v}_{\mathrm{AB}} \cdot \tau_{\mathrm{A}}^{\mathrm{B}} = \boldsymbol{s}(t_1) + \boldsymbol{v}_{\mathrm{AB}} \cdot (\tau_{\mathrm{d}} + \tau_{\mathrm{A}}^{\mathrm{B}}) \quad (3)$$

where $\boldsymbol{v}_{\mathrm{AB}}$ indicates the radial relative motion velocity vector between satellites, $\tau_{\mathrm{d}} = t_2 - t_1$. ISD vector $\boldsymbol{s}(t_1)$ can be expressed as

$$\boldsymbol{s}(t_3) - \boldsymbol{s}(t_2) + \boldsymbol{v}_{\mathrm{AB}} \cdot \tau_{\mathrm{A}}^{\mathrm{B}} = \boldsymbol{s}(t_1) + \boldsymbol{v}_{\mathrm{AB}} \cdot (\tau_{\mathrm{d}} + \tau_{\mathrm{A}}^{\mathrm{B}}). \quad (4)$$

Use the velocity vector and the propagation delay product to represent the satellite flight vector as

$$\rho = |\boldsymbol{s}(t_3)| - \frac{\boldsymbol{v}_{\mathrm{AB}}^{\mathrm{T}} \cdot (\tau_{\mathrm{d}} + \tau_{\mathrm{A}}^{\mathrm{B}}) + \dot{\boldsymbol{r}}_{\mathrm{A}}(t_1)\widehat{\boldsymbol{e}}_{\mathrm{AB}}(t_1) \cdot \tau_{\mathrm{B}}^{\mathrm{A}}}{2} - \frac{\dot{\boldsymbol{r}}_{\mathrm{B}}(t_3)\widehat{\boldsymbol{e}}_{\mathrm{AB}}(t_3)\tau_{\mathrm{A}}^{\mathrm{B}}}{2} \quad (5)$$

where $\dot{\boldsymbol{r}}_{\mathrm{A}}(t_1)$ is the velocity of SA at t_1 and $\dot{\boldsymbol{r}}_{\mathrm{B}}(t_3)$ is the velocity of SB at t_3, $\widehat{\boldsymbol{e}}_{\mathrm{AB}}(t_i)$ represents the ISD unit vector of the no-minal time t_i.

$\eta_{\mathrm{A}} = \dot{\boldsymbol{r}}_{\mathrm{A}}(t_1)\widehat{\boldsymbol{e}}_{\mathrm{AB}}(t_1)$ and $\eta_{\mathrm{B}} = \dot{\boldsymbol{r}}_{\mathrm{B}}(t_3)\widehat{\boldsymbol{e}}_{\mathrm{AB}}(t_3)$ are, respectively, the velocity component of $\boldsymbol{s}(t_1)$ and the velocity component of $\boldsymbol{s}(t_3)$. Therefore, ρ can be written as

$$\rho = |\boldsymbol{s}(t_3)| - \frac{\boldsymbol{v}_{\mathrm{AB}} \cdot (\tau_{\mathrm{d}} + \tau_{\mathrm{A}}^{\mathrm{B}}) + \eta_{\mathrm{A}}\tau_{\mathrm{B}}^{\mathrm{A}} - \eta_{\mathrm{B}}\tau_{\mathrm{A}}^{\mathrm{B}}}{2}. \quad (6)$$

Therefore, the ISD calculated by the dual one-way ranging formula settlement is equal to the instantaneous ISD minus the systematic error introduced by the dynamic motion of the satellite. In the expression of systematic error, it can be seen that the magnitude of the error term depends

on the orbit of the satellite and τ_{d}, and the larger the τ_{d}, the larger the error.

When the maximum ISD $S_{\max}=4\,000$ km, $\tau=13.3$ ms, $\boldsymbol{v}_{\mathrm{AB}}=3$ km/s, $\tau_{\mathrm{d}}=1$ s, the system error caused by the dynamic motion of the satellite is 1 520 m with quantitative analysis.

2.2.2 Frequency source drift error

When analyzing the influence of frequency source drift on measurement accuracy, the effects of ionospheric delay and hardware transmission delay are temporarily ignored, and it is assumed that the propagation delays of the measurement links $\boldsymbol{S}_{\mathrm{B}}^{\mathrm{A}}$ and $\boldsymbol{S}_{\mathrm{B}}^{\mathrm{A}}$ are equal, that is, $\tau_{\mathrm{A}}^{\mathrm{B}}=\tau_{\mathrm{B}}^{\mathrm{A}}=\tau$. The nominal moments of SA emission time, SB reception time, SB transmission time, and SA reception time are defined as time nodes 0, 1, 2, and 3, and the time node 0 is set to $t=0$.

In the measurement process, each satellite obtains the transmission time of the signal by making the local pseudo-code phase different from the pseudo-code phase received by the received pseudo-code phase. Considering the influence of frequency source drift, the instantaneous frequencies of SA and SB are

$$f_{\mathrm{A}}(t)=f_{\mathrm{c}}+\alpha_0+\int_0^t\alpha_1(\tau)\mathrm{d}\tau, \tag{7}$$

$$f_{\mathrm{B}}(t)=f_{\mathrm{c}}+\beta_0+\int_0^t\beta_1(\tau)\mathrm{d}\tau. \tag{8}$$

$\theta_A(t)$ and $\theta_B(t)$ are the local pseudo code phase signals of SA and SB, f_{c} is the nominal pseudo code rate of SA and SB, $\alpha_0+\int_0^t\beta_1(\tau)\mathrm{d}\tau$ and $\beta_0+\int_0^t\beta_1(\tau)\mathrm{d}\tau$ are the frequency drift functions of SA and SB respectively.

Define the phases of the A and B pseudo codes of the node n in the random access network are θ_{A_n} and θ_{B_n} respectively, and then the pseudo-code phase of SA at node 3 is

$$\theta_{\mathrm{A}\_3}=\theta_{\mathrm{A}\_0}+\int_0^{\tau_{\mathrm{d}}+2\tau}(f_{\mathrm{c}}+\alpha_0+\int_0^t\alpha_1(\tau)\mathrm{d}\tau)\mathrm{d}t. \tag{9}$$

The pseudo-code phases of the same SB at node 1 and node 2 are

$$\theta_{\mathrm{B}\_1}=\theta_{\mathrm{B}\_0}+\int_0^{\tau}(f_{\mathrm{c}}+\beta_0+\int_0^t\beta_1(\tau)\mathrm{d}\tau)\mathrm{d}t, \tag{10}$$

$$\theta_{\mathrm{B}\_2}=\theta_{\mathrm{B}\_0}+\int_0^{\tau_{\mathrm{d}}+\tau}(f_{\mathrm{c}}+\beta_0+\int_0^t\beta_1(\tau)\mathrm{d}\tau)\mathrm{d}t. \tag{11}$$

SA receives the pseudo-code signal sent by SB at node 2 and node 3, extracts the pseudo-code phase of the received signal, and then compares it with the local pseudo-code phase to obtain the pseudo-code phase difference.

$$\theta_{\mathrm{A}}^{\mathrm{B}}=\theta_{\mathrm{A}\_3}-\theta_{\mathrm{B}\_2}=$$

$$\theta_{\mathrm{A}\_0}-\theta_{\mathrm{B}\_0}+(f_{\mathrm{c}}+\alpha_0)\tau+(\alpha_0-\beta_0)(\tau_{\mathrm{d}}+\tau)+$$

$$\int_0^{\tau_{\mathrm{d}}+2\tau}\int_0^t\alpha_1(\tau)\mathrm{d}\tau\mathrm{d}t-\int_0^{\tau_{\mathrm{d}}+\tau}\int_0^t\beta_1(\tau)\mathrm{d}\tau\mathrm{d}t. \tag{12}$$

The signal propagation delay does not exceed 17 ms at most, and the drift functions $\alpha_1(t)$ and $\beta_1(t)$ are functions that change very slowly. Therefore, the drift function $\alpha_1(t)$ and $\beta_1(t)$ can be considered constants in the time of one measurement process.

$$\begin{cases}\alpha_1(t)=\alpha_1\\ \beta_1(t)=\beta_1\end{cases} \tag{13}$$

The ISD solved by the dual one-way ranging formula can be expressed as

$$\rho=\frac{\theta_{\mathrm{B}}^{\mathrm{A}}+\theta_{\mathrm{A}}^{\mathrm{B}}}{2f_{\mathrm{c}}}\cdot\mathrm{c}=$$

$$\mathrm{c}\tau+\frac{(\alpha_0+\beta_0)\tau+(\alpha_0-\beta_0)(\tau_{\mathrm{d}}+\tau)\mathrm{c}}{2f_{\mathrm{c}}}+$$

$$\frac{\alpha_1(\tau_{\mathrm{d}}+2\tau)^2\mathrm{c}-\beta_1(2\tau_{\mathrm{d}}\tau+\tau_{\mathrm{d}}^2)}{4f_{\mathrm{c}}}. \tag{14}$$

The measurement error is quantified without applying the interpolation algorithm. Taking the 40 MHz and 1 ppm crystal as an example, the frequency drift parameter has a value range of

$$\begin{cases}\alpha_0\in[-40,+40]\\ \beta_0\in[-40,+40]\\ \alpha_1\in[-1,+1]\\ \beta_1\in[-1,+1]\end{cases}. \tag{15}$$

When $\tau_{\mathrm{d}}=1$ s, $\alpha_0=40$ Hz, $\beta_0=-40$ Hz, $\alpha_1=1$ Hz/s, $\beta_1=1$ Hz/s, the ISD measurement error caused by frequency source drift is 303.75 m.

3. Ranging accuracy optimization and simulation

3.1 Ranging precision principle

In the RAISR system, due to different characteristics of transmission and reception, the error caused by the dynamic motion of the satellite and the drift of the frequency source is amplified. This paper proposes to use the interpolation algorithm to correct the time. The interpolation algorithm is based on pseudo-range. The observation itself calculates different moments of the measurement, and corrects the measured value at a certain moment to another time, effectively eliminating the systematic error caused by the dynamic motion of the satellite and the drift of the frequency source.

For two satellites that are ranging from each other, the polynomial interpolation method is shown in Fig. 3.

In Fig. 3, SA emits a signal at its clock face time T_0.

SB receives the signal and measures the one-way ranging result ρ_{B1}. SB transmits a signal at its clock face time T_2. SA receives a signal and measures the one-way ranging result ρ_{A1}. With the number of signals transmitted by SA and SB increasing, SA and SB respectively obtain the one-way ranging results $(\rho_{\mathrm{A1}}, \rho_{\mathrm{A2}}, \rho_{\mathrm{A3}}, \ldots, \rho_{\mathrm{A}M})$ and $(\rho_{\mathrm{B1}}, \rho_{\mathrm{B2}}, \rho_{\mathrm{B3}}, \ldots, \rho_{\mathrm{B}N})$. The moments at which SA and SB transmit signals are random, so the obtained ranging results are not equally spaced. In Fig. 3(b), the polynomial interpolation method refers to fitting the pseudo-range value corresponding to the clock time of SB receiving time by using the actually measured pseudo-range $(\rho_{\mathrm{A1}}, \rho_{\mathrm{A2}}, \rho_{\mathrm{A3}}, \ldots, \rho_{\mathrm{A}M})$, for example, $\rho_{\mathrm{A}}(T_1)$ corresponding to time T_1 of SA clock face time, as shown by the red dotted line in the figure, the bidirectional pseudo-range observation $(\rho_{\mathrm{A}}(T_1), \rho_{B1})$ that has been subjected to polynomial interpolation is used to solve the ISD. Similarly, SB uses the ranging result $(\rho_{\mathrm{B1}}, \rho_{\mathrm{B2}}, \rho_{\mathrm{B3}}, \ldots, \rho_{\mathrm{B}N})$ to fit the pseudo-range $(\rho_{\mathrm{B}}(T_3), \rho_{\mathrm{B}}(T_5), \rho_{\mathrm{B}}(T_{11}), \rho_{\mathrm{B}}(T_{15}), \rho_{\mathrm{B}}(T_{17}), \ldots)$, which corresponds to the clock face time of SA. We can calculate the fitted values and measured values. That is to say, a bidirectional distance measurement can be completed every time a satellite sends a signal by polynomial interpolation.

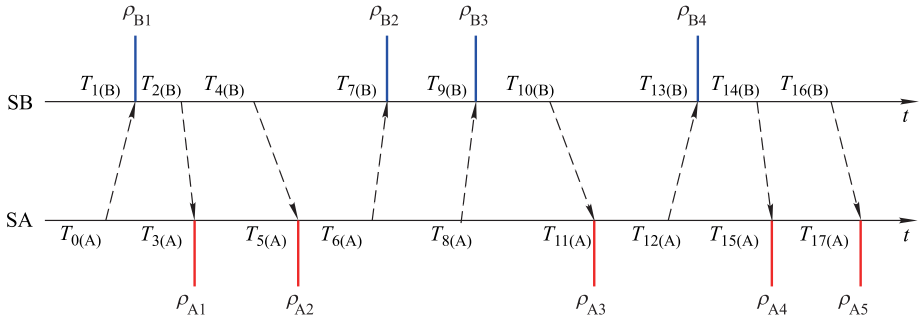

(a) Dual one-way ranging of SA and SB

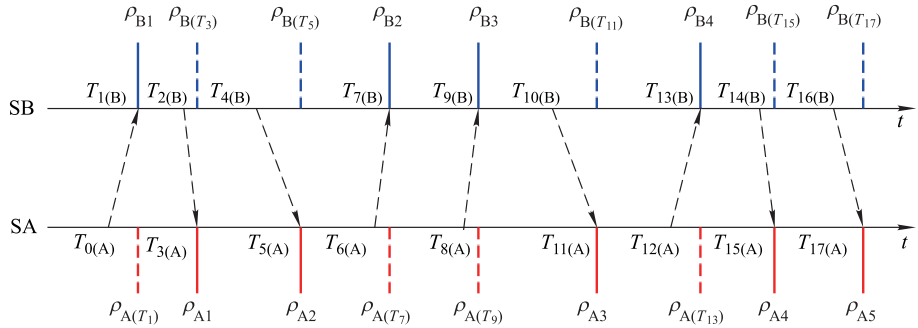

(b) Polynomial interpolation

Fig. 3 Algorithm based on polynomial interpolation

3.2 Capture method

The fast acquisition method of direct spread spectrum signals by the physical layer is delay multiplication. The influence of Doppler frequency offset can be eliminated by multiplying the received signal with the conjugate signal delayed by itself. The received pseudo-code phase can be calculated quickly by fast Fourier transform (FFT). The principle block diagram is shown in Fig. 4.

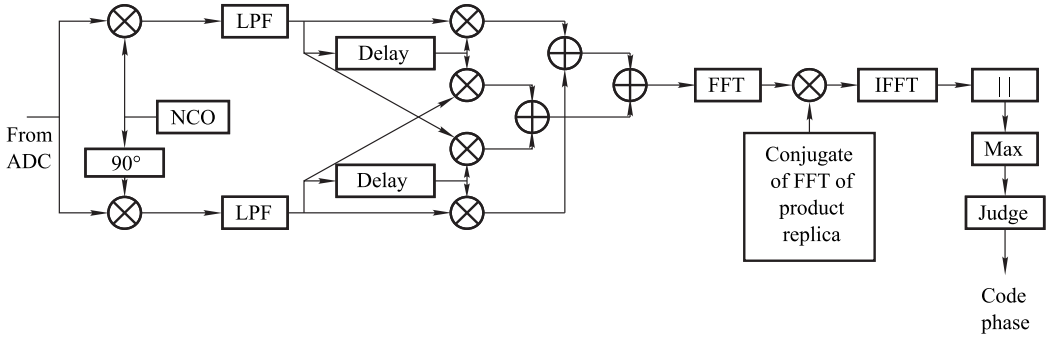

Fig. 4 Delay and multiplication method block diagram

The digital intermediate frequency signal output by the analog-to-digital converter (ADC) is multiplied by its delayed complex conjugate after being down-mixed and low-pass filtered. LPF is short for low pass filter. NCO is short for numerically controlled oscillator. IFFT is short for inverse fast Fourier transform. The local pseudo-code is multiplied by its delayed local pseudo-code signal, and then the two are related to the frequency domain code phase search. The received intermediate frequency signal output by the ADC can be expressed as

$$r(nT_{\rm s}) = \sqrt{2P}{\rm c}(nT_{\rm s}-\tau)\cdot$$
$$\cos(2\pi(f_{\rm IF}+f_{\rm d})nT_{\rm s}+\theta_0)+w(nT_{\rm s}) \tag{16}$$

where P is the received signal power, $T_{\rm s}$ is the sampling period, $nT_{\rm s}$ is the sampling time, ${\rm c}(nT_{\rm s}-\tau)$ is the pseudo-code sequence, τ is the unknown delay, and $f_{\rm IF}, f_{\rm d}$ and θ_0 are the nominal intermediate frequency of the carrier, the Doppler frequency and the initial phase. $w(nT_{\rm s})$ represents Gaussian white noise and obeys the normal distribution $N(0,\sigma_2)$. The received intermediate frequency signal is digitally down-mixed with the local carrier, and then the high-frequency component is filtered through a low-pass filter. The output I and Q low-frequency components are expressed as

$$r_{\rm I}(nT_{\rm s}) = \sqrt{P}{\rm c}(nT_{\rm s}-\tau)\cos(2\pi f_{\rm d}nT_{\rm s}+\theta_0)+w_{\rm I}(nT_{\rm s}), \tag{17}$$

$$r_{\rm Q}(nT_{\rm s}) = \sqrt{P}{\rm c}(nT_{\rm s}-\tau)\sin(2\pi f_{\rm d}nT_{\rm s}+\theta_0)+w_{\rm Q}(nT_{\rm s}), \tag{18}$$

where $w_{\rm I}(nT_{\rm s})$ and $w_{\rm Q}(nT_{\rm s})$ represent noise terms. The two signals are delayed by an integer number of chip times. The delay time is expressed as $kT_{\rm s}$, k is a fixed constant, and then the delay amount is conjugated and multiplied by the undelayed signal component, because the delay amount k is a fixed constant. After the delay multiplication process, the Doppler frequency in the obtained signal is eliminated, leaving only the pseudo-code signal and noise. Then, the phase of the received pseudo-code is directly obtained by the FFT. After obtaining the pseudo-code phase and compensating the local pseudo-code signal, the local pseudo-code is used to despread the received direct-spread spectrum (DS) signal to obtain a single carrier, and then the Doppler frequency of the carrier can be directly calculated to complete the capture of the received signal.

3.3 Simulation

The interpolation algorithm eliminates the error caused by the dynamic motion of the satellite, greatly reduces the error caused by the drift of the frequency source, but introduces the interpolation error. The magnitude of the interpolation error is related to the sampling interval and the polynomial order. This article uses the Satellite Tool Kits (STK) to generate ISD simulation data for numerical analysis of interpolation errors. The satellite orbit is set to J4 perturbation and low earth orbit (LEO). The two satellites are located in different orbits. The duration of the simulated data is 1 h, and the interval is 0.05 s. Using this ISD simulation data, the interpolation precisions for different sample sampling intervals and different polynomial orders are calculated separately. In this paper, the difference accuracy is evaluated by the maximum error and the root mean square error (MSE). The distance between the lines is taken as the true value, the interpolation value P at the time of the difference is compared with the corresponding ISD analog value $P_{\rm true}$, and the interpolation error ΔP is obtained.

$$\Delta P = P - P_{\rm true} \tag{19}$$

The commonly used indicators for evaluating the accuracy of the difference are the maximum error and the root MSE. The formula for calculating the root MSE is

$$\Delta P_{\rm rms} = \sqrt{\frac{1}{N}\sum_{k=1}^{N}|\Delta P_k|^2}. \tag{20}$$

The ISD simulation values are sampled at an average sampling interval of 0.5 s, 0.6 s, 0.7 s, 4.9 s, and 5 s, and the 2nd-order to the 8th-order Lagrange polynomial interpolation (LPI) precision is calculated. The maximum error of statistical interpolation is root MSE. In each case, 100 times value calculation and statistical results, the uniform interval sampling and non-uniform interval sampling calculation results are shown in Fig. 5 – Fig. 11.

Through statistical comparison analysis, under the same conditions, the interpolation error of equally spaced samples is smaller than that of non-uniform interval sampling. When the average sampling interval of non-uniform interval samples is less than 2 s, the interpolation polynomial order should select a smaller value, and the 2nd- or 3rd-order is more suitable. The average sampling interval is in the range of 2 s to 5 s, and the interpolation polynomial order is the 4th-order. That is to say, when the satellite system measurement task is frequent, the interpolation algorithm adopts the 2nd- or 3rd-order to bring a smaller error. When the system has fewer measurement tasks, the 4th-order interpolation algorithm has a smaller error. Using the results of the analysis to perform polynomial interpolation on the system allows the interpolation error to be controlled in the order of millimeter.

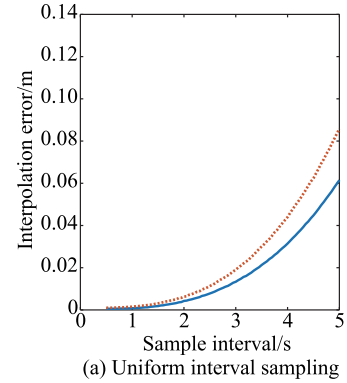

(a) Uniform interval sampling

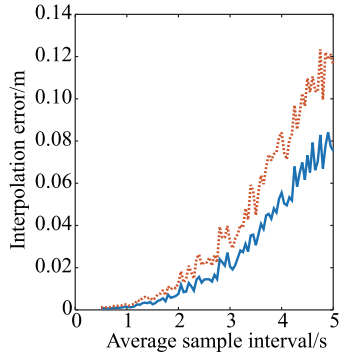

(b) Non-uniform interval sampling

—— : Root MSE; ····· : The maximum error.

Fig. 5 The 2nd-order LPI

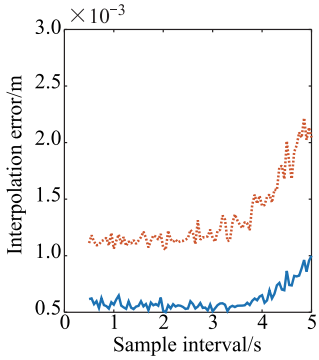

(a) Uniform interval sampling

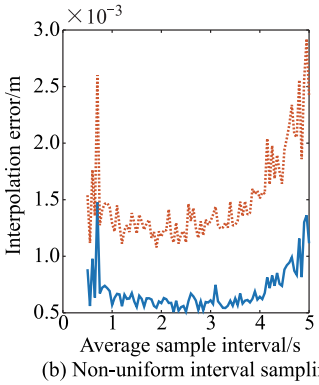

(b) Non-uniform interval sampling

—— : Root MSE; ····· : The maximum error.

Fig. 6 The 3rd-order LPI

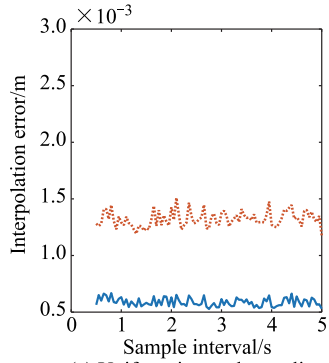

(a) Uniform interval sampling

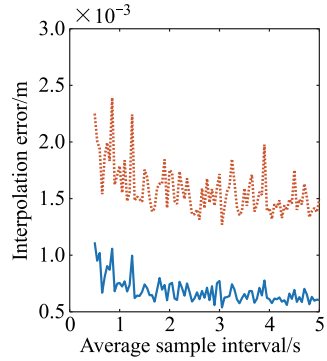

(b) Non-uniform interval sampling

—— : Root MSE; ····· : The maximum error.

Fig. 7 The 4th-order LPI

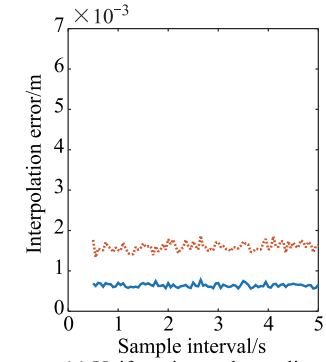

(a) Uniform interval sampling

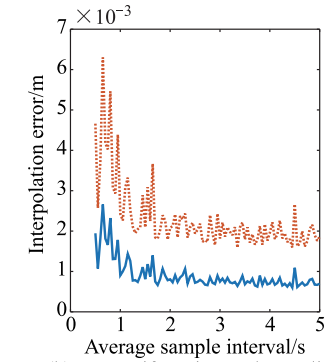

(b) Non-uniform interval sampling

—— : Root MSE; ····· : The maximum error.

Fig. 8 The 5th-order LPI

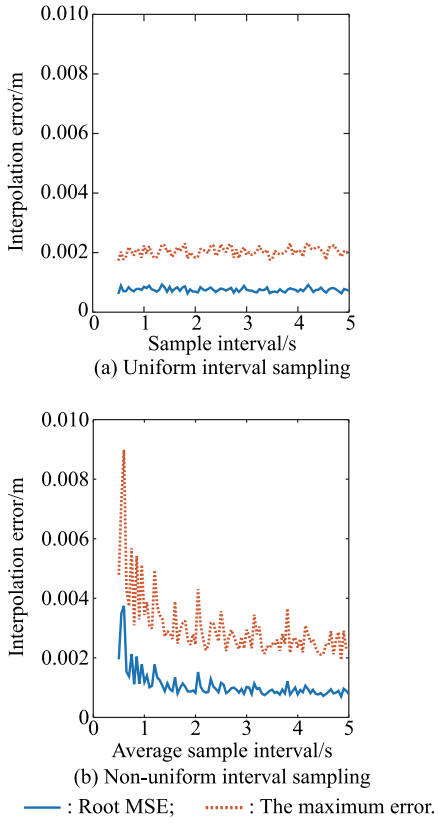

Fig. 9 The 6th-order LPI

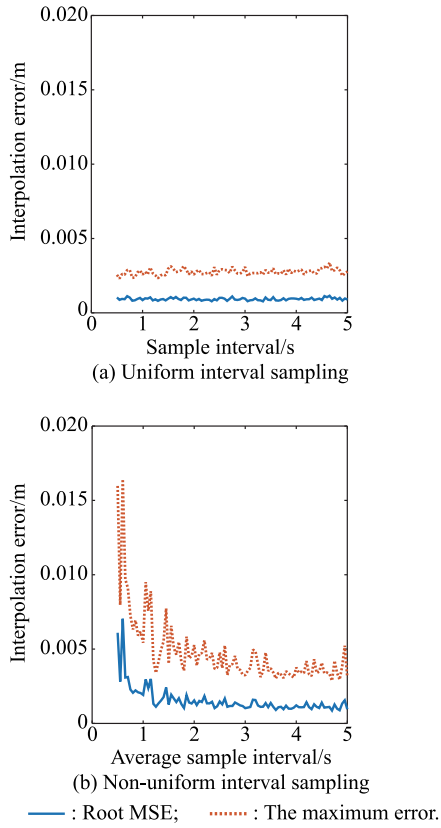

Fig. 10 The 7th-order LPI

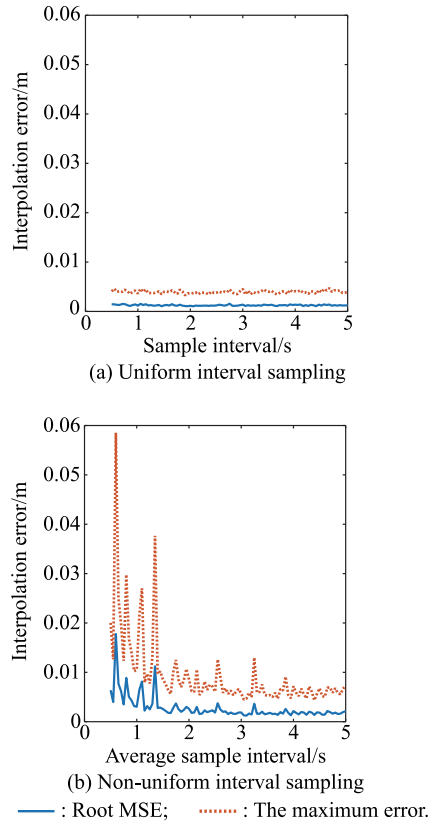

Fig. 11 The 8th-order LPI

4. System demonstration

The physical map of the ranging platform of the RAISR system is shown in Fig. 12, and its connection relationship is shown in Fig. 13. The current test platform contains a total of three satellites, and the satellites are connected by radio frequency (RF) cables and RF connectors. The output signal of each satellite is split into two paths by a splitter, which are connected to the combiner of the other two satellites, thus ensuring the connection between any two satellites. Each satellite transmits the distance measurement value to the personal computer (PC) through the universal asynchronous receiver/transmitter (UART) interface, and the ISD is solved by the PC.

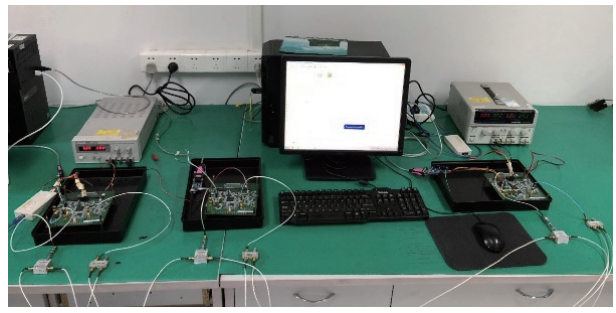

Fig. 12 Test bench

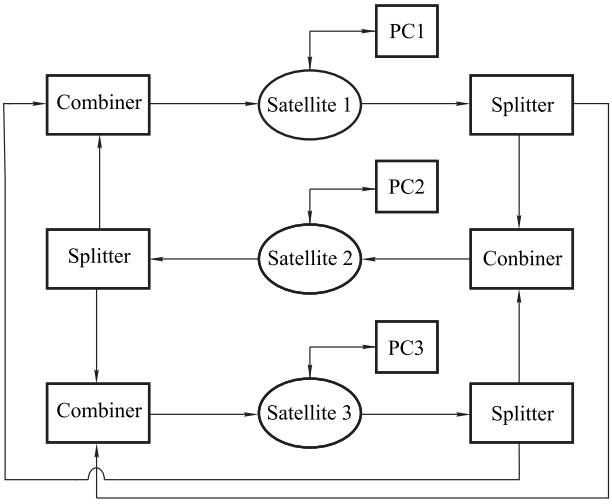

Fig. 13 Connection relationship

The hardware platform of the inter-satellite communication measurement system designed in this paper is a new generation of miniature measurement and control transponder developed by the research group. Its structure is shown in Fig. 14. The RF transmit front end and the RF receive front end have only amplifiers and RF filters, which function to filter and amplify the RF signal. The functions of downmixing, analog wideband automatic gain control (AGC) processing, analog-to-digital conversion, digital-to-analog conversion, and up-conversion are all performed in the baseband single chip. The digital processing module is responsible for signal synchronization, relative ranging, performing multiple access protocols, protocol data packets, etc., and is implemented in a Xilinx field programmable gate array (FPGA). Fig. 15 is the workflow of the inter-satellite ranging system.

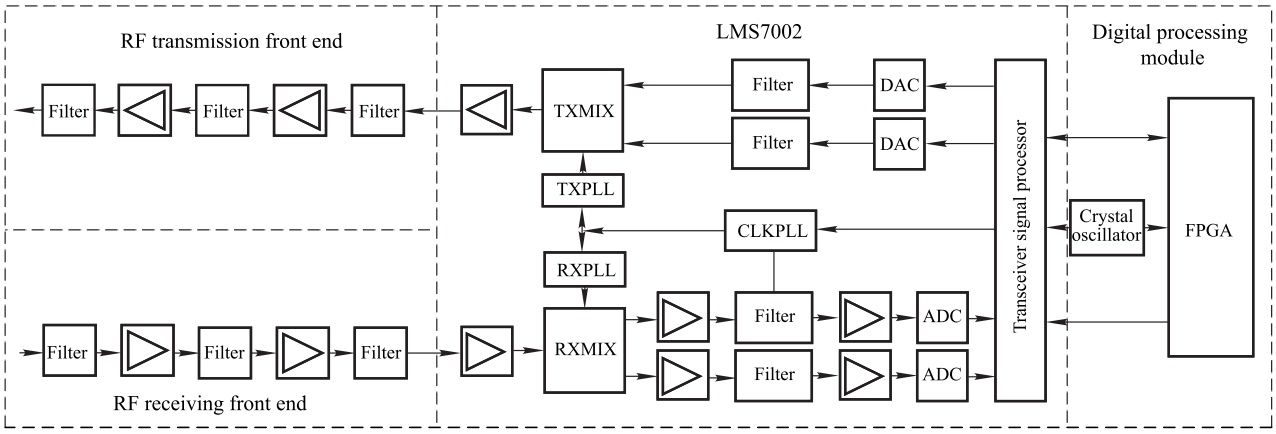

Fig. 14 Hardware platform structure functional block diagram

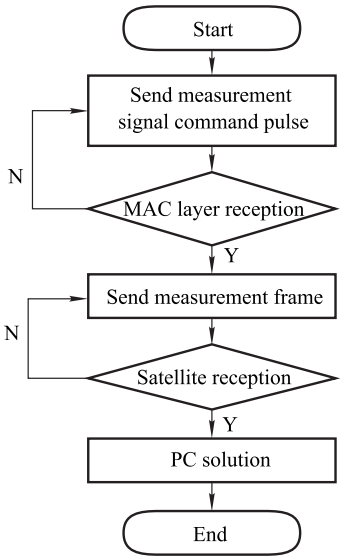

Fig. 15 Workflow of inter-satellite ranging system

Step 1 The application layer sends the measurement signal command pulse.

Step 2 The media access control (MAC) layer receives the measurement command pulse.

Step 3 The MAC layer successfully contends to the channel and sends a complete measurement frame.

Step 4 After receiving the measurement signal, the satellite samples the measurement signal and transmits it to the PC.

Step 5 The distance is calculated by PC.

When the epoch reduction is not performed, the ISD solution is to add the two mutually opposite but distance measurement values with the shortest bidirectional measurement interval (BMI). As shown in Fig. 16, SB receives the measurement signal of the SA emission. The one-way distance values are ρ_{B1}, ρ_{B2} and ρ_{B3}. SA receives the measurement signals transmitted by SB to obtain the one-way distance values ρ_{A1} and ρ_{A2}. For ρ_{A1}, the inverse ranging value with which the measurement time interval is the smallest is ρ_{B1}, so ρ_{A1} and ρ_{B1} are added to calculate the

ISD value. Similarly, ρ_{A2} and ρ_{B3} are combined into a pair of mutually opposite distance measurements. ρ_{B2} in Fig. 16 is discarded and not used for solving the ISD.

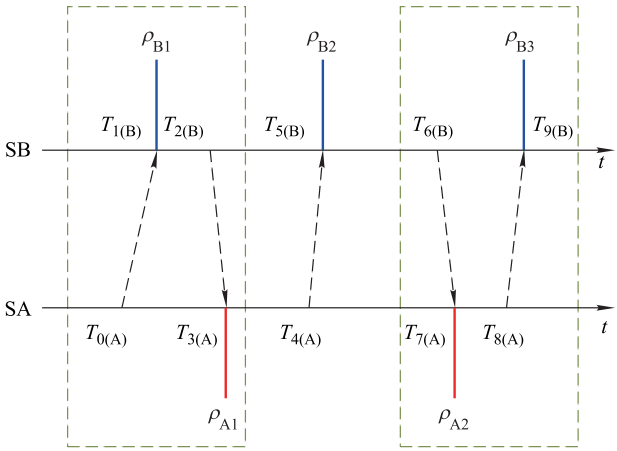

Fig. 16 ISD solving method

The nominal frequency of the crystal oscillator used in the system is 40 MHz, and the command average generation rate $\lambda = 1$. By testing the actual frequency accuracy of the crystal oscillator, the maximum frequency deviation between different crystal oscillators is about 60 Hz. After 2 s, the time deviation of the two crystals can reach 3 μs.

The crystal oscillator time deviation is converted to a bidirectional distance deviation of 450 m. Fig. 17 shows the maximum BMI of 2.65 s. The corresponding ISD value is 412.6 m, and the measured ISD is 799.1 m, that is, the maximum ranging error is about 386.5 m. That is to say, the actual ranging error is within the range of the theoretical deviation.

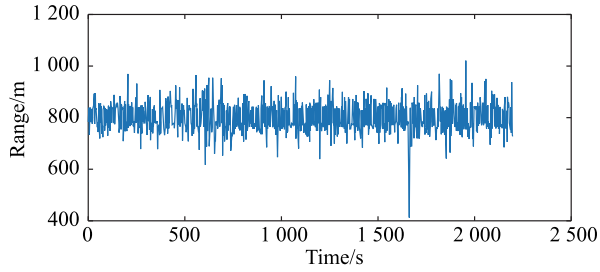

(a) ISD between SA and SB

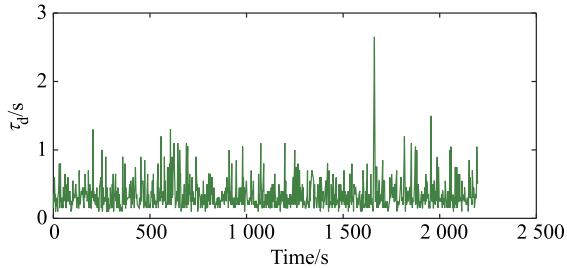

(b) BMI

Fig. 17 $\mathrm{ISD_{A-B}}$ and $\mathrm{BMI_{A-B}}$

Fig. 18 shows the relationship between $\mathrm{ISD_{B-C}}$ and the corresponding time interval. Fig. 19 shows the relationship between $\mathrm{ISD_{C-A}}$ and the corresponding time interval.

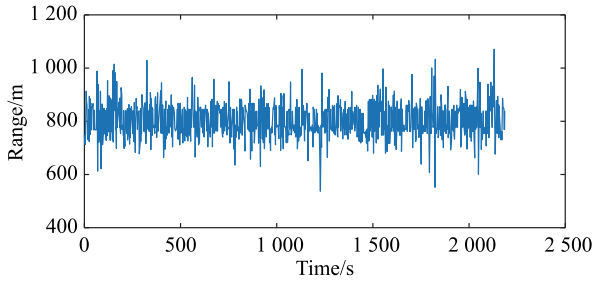

(a) ISD between SB and SC

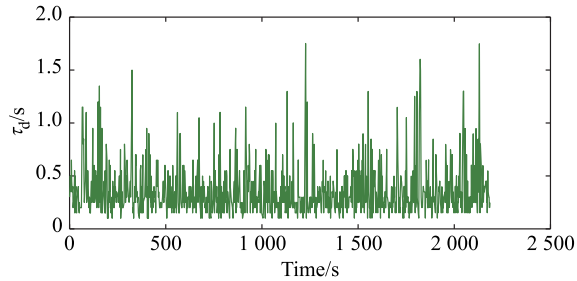

(b) BMI

Fig. 18 $\mathrm{ISD_{B-C}}$ and $\mathrm{BMI_{B-C}}$

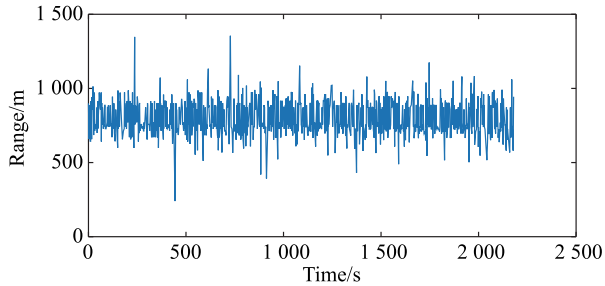

(a) ISD between SC and SA

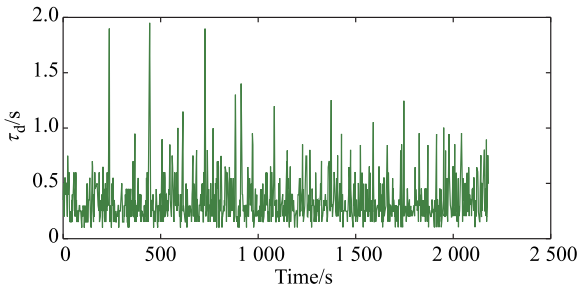

(b) BMI

Fig. 19 $\mathrm{ISD_{C-A}}$ and $\mathrm{BMI_{C-A}}$

In the case of no optimization of ranging performance, the two-way ranging method based on random access has an MSE of several tens of meters or even more than one hundred meters, which is shown in Table 1.

Table 1 Ranging error

Distance	λ/s	MSE/m
$S_{\mathrm{A-B}}$	0.337	56.158
$S_{\mathrm{B-C}}$	0.349	63.640
$S_{\mathrm{C-A}}$	0.333	114.353

Fig. 20 shows the ISD solving method using epoch reduction.

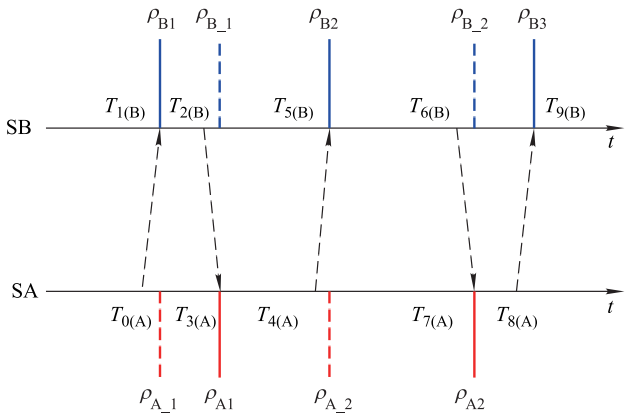

Fig. 20 ISD solving method using epoch reduction

After the epoch reduction, the measurement results between the satellites are shown in Fig. 21. Fig. 21(a) is the ISD value calculated by the combination of the measured distance value of SA and the interpolation distance of SB, denoted as $S_{\mathrm{A-B}}$. Fig. 21(b) is the ISD value calculated by the combination of the measured distance value of SB and the interpolation distance of SA, and is recorded as $S_{\mathrm{B-A}}$. As can be seen from comparison with Fig. 17(a), after the epoch reduction, the ranging error is significantly reduced.

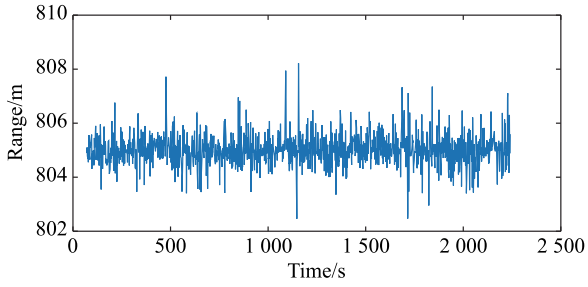

(a) ISD between SB and SC

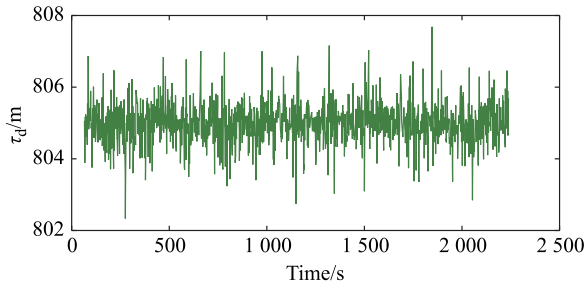

(b) BMI

Fig. 21 Ranging value of SA and SB after epoch reduction

Table 2 lists the distance values between any two satellites in the network consisting of three satellites after epoch reduction. It can be seen that when the average time interval between the actual signals transmitted by each satellite is about 1.21 s, the ranging accuracy after the aging of the epochs is in the range of 0.762 m to 1.043 m.

Table 2 Distance error after epoch reduction

Distance	$S_{\mathrm{A-B}}$	$S_{\mathrm{B-A}}$	$S_{\mathrm{B-C}}$	$S_{\mathrm{C-B}}$	$S_{\mathrm{C-A}}$	$S_{\mathrm{A-C}}$
MSE/m	0.567	0.562	0.451	0.471	0.509	0.569

It is found that the actual measurement results are deviated from the simulation results. After analysis, it is considered that the time used for the simulation is a more accurate system time. In actual measurement, since the system has no time synchronization, the clock time is different. The interpolation time includes the receiver measurement error, so we carried out the homologous experiment. The three satellites in the network are driven by the same frequency source, and the zero time of the three satellites is kept consistent by resetting. In this state, there is no longer a ranging error caused by the frequency source offset in the system. Fig. 22(a) shows the ISD between SA and SB, and Fig. 22(b) shows the BMI corresponding to each distance value.

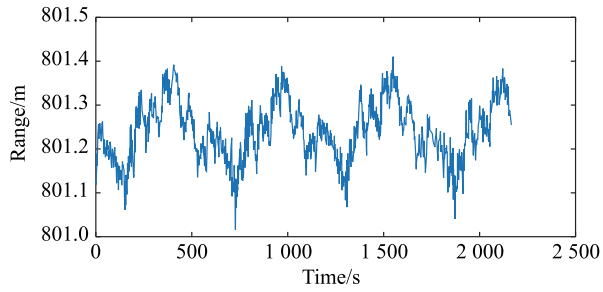

(a) ISD between SA and SB

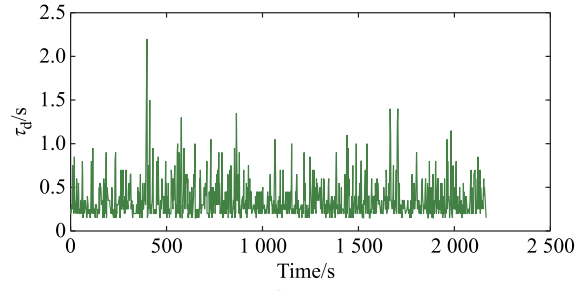

(b) BMI

Fig. 22 Ranging results of SA and SB in homologous experiments

It is statistically obtained that the ranging MSE at this time is 0.069 m. The interpolated ranging value is basically the same as the ranging variance before unplugged, indicating the interpolate on error in the case of time synchronization. It is less than the thermal noise and the ranging error caused by the internal digital processing of the

system. In the absence of time synchronization, the deviation between the actual test result and the theoretical result is mainly caused by the interpolation error.

5. Conclusions

In this paper, we design the RAISR system and analyze the system accuracy by simulation quantitatively. An accuracy optimization approach to the RAISR system is proposed, which eliminates the error caused by the two-way ranging time interval. The physical system test results show that the MSE is reduced from the maximum 114.353 m to 0.069 m, and the accuracy is improved by 99.94%. The ranging accuracy of the RAISR system is demonstrated in the numerical simulation and hardware platform tests.

References

[1] MAURICE M, STALLARD M. Distributed satellite missions and technologies — The TechSat 21 program. Proc. of the Space Technology Conference and Exposition, 1999: 1 – 8.

[2] DEL PORTILLO I, CAMERON B G, CRAWLEY E F. A technical comparison of three low earth orbit satellite constellation systems to provide global broadband. Acta Astronautica, 2019, 159(6): 123 – 135.

[3] LEE J, LUU T, KONANGI V. Design of a satellite cluster system in distributed simulation. Simulation, 2005, 81(1): 57 – 66.

[4] SABOL C, BURNS R, MCLAUGHLIN C A. Satellite formation flying design and evolution. Journal of Spacecraft and Rockets, 2001, 38(2): 270 – 278.

[5] BAKSHI K. Considerations for software defined networking (SDN): approaches and use cases. Proc. of the IEEE Aerospace Conference, 2013: 1 – 9.

[6] GUNGOR V C, LU B, HANCKE G P. Opportunities and challenges of wireless sensor networks in smart grid. IEEE Trans. on Industrial Electronics, 2010, 57(10): 3557 – 3564.

[7] GUNDERSON A, KLUMPAR D, CRAWFORD A, et al. Simultaneous multi-point space weather measurements using the lowcost EDSN cubesat constellation. https:// digitalcommons.usu.edu/smallsat/2013/all2013/39/.

[8] COCKRELL J, ALENA R, MAYER D, et al. EDSN: a large swarm of advanced yet very affordable, COTS-based nanosats that enable multipoint physics and open source apps. Proc. of the 26th Annual AIAA/USU Conference on Small Satellites, 2012: 1 – 12.

[9] SHAW A W, HEINKE C O, MACCARONE J J, et al. The swift bulge survey: optical and near-IR follow-up featuring a likely symbiotic X-ray binary and a focused wind CV. Monthly Notices of the Royal Astronomical Society, 2020, 492(3): 4344 – 4360.

[10] LLORENTE J S, AGENJO A, CARRASCOSA C, et al. PROBA-3: precise formation flying demonstration mission. Acta Astronautica, 2013, 82(1): 38 – 46.

[11] RUIZ DE AZUA J A, CALVERAS A, CAMPS A. Internet of satellites (IoSat): an interconnected space paradigm. Proc. of the 5th International Federated and Fractionated Satellite Systems Workshop, 2017: 1 – 8.

[12] SELVA D, GOLKAR A, KOROBOVA O, et al. Distributed earth satellite systems: what is needed to move forward. Journal of Aerospace Information Systems, 2017, 14(8): 412 – 438.

[13] FABER N, NAKAMURA Y, ALENA R, et al. Heterogeneous spacecraft networks: general concept and case study of a cost-effective, multi-institutional earth observation platform. Proc. of the Aerospace Conference, 2014: 1 – 16.

[14] RUIZ DE AZÚA J A, CALVERAS A, CAMPS A. Internet of satellites (IoSat): analysis of network models and routing protocol requirements. IEEE Access, 2018, 6: 20390 – 20411.

[15] ALESSANDRO A. Architecting federated satellite systems for successful commercial implementation. Proc. of the AIAA Space Conference & Exposition, 2013: 1 – 17.

[16] ZHEN L, QIN H, ZHANG Q, et al. Optimal preamble design in spatial group-based random access for satellite-M2M communications. IEEE Wireless Communications Letters, 2019, 8(3): 953 – 956.

[17] WU S F, CHEN W, ZHANG Y H, et al. SULFRO: a swarm of nano-/micro-sat SE l2 for space ultra-low frequency radio observatory. Proc. of the 28th Annual AIAA/USU Conference on Small Satellites, 2014: 1 – 9.

[18] GAUDENZI R D, HERRERO O D R, GALLINARO G, et al. Random access schemes for satellite networks, from VSAT to M2M: a survey. International Journal of Satellite Communications and Networking, 2018, 36(1): 66 – 107.

[19] ZHEN L, SUN T, LU G Y, et al. Preamble design and detection for 5G enabled satellite random access. IEEE Access, 2020, 8: 49873 – 49884.

[20] ZHAO B, REN G L, ZHANG H N. Multisatellite cooperative random access scheme in low earth orbit satellite networks. IEEE Systems Journal, 2019, 13(3): 2617 – 2628.

[21] ZHU H, CHEN S Y, LI F H, et al. User random access authentication protocol for low earth orbit satellite networks. Journal of Tsinghua University (Science and Technology), 2019, 59(1): 1 – 8.

[22] HITOMI N, BANG H, SELVA D. Adaptive knowledge-driven optimization for architecting a distributed satellite system. Journal of Aerospace Computing, Information and Communication, 2018, 15(8): 485 – 500.

[23] RUIZ DE AZUA J A, CALVERAS A, GOLKAR A, et al. Proof-of-concept of a federated satellite system between two 6-unit CubeSats for distributed earth observation satellite systems. Proc. of the 7th International Geoscience and Remote Sensing Symposium, 2019: 8871 – 8874.

[24] HU X Z, ZHAO Y, CHEN X Q, et al. Conceptual moon imaging micro/nano-satellite design optimization under uncertainty. Acta Astronautica, 2018, 148(7): 22 – 31.

[25] REN X, YANG Y X, ZHU J, et al. Comparing satellite orbit determination by batch processing and extended Kalman filtering using inter-satellite link measurements of the next-generation BeiDou satellites. GPS Solutions, 2019. DOI: 10.1007/s10291-018-0816-9.

[26] AMANOR D N, EDMONSON W W, AFGHAH F. Intersatellite communication system based on visible light. IEEE Trans. on Aerospace and Electronic Systems, 2018, 54(6): 2888 – 2899.

[27] PAN L, ZHANG X H, LI X X, et al. Satellite availability and point positioning accuracy evaluation on a global scale for integration of GPS, GLONASS, BeiDou and Galileo. Advances in Space Research, 2019, 63(9): 2696 – 2710.

[28] SHEN C C, RAJAGOPALAN S, BORKAR G, et al. A flexible routing architecture for ad hoc space networks. Computer Networks, 2004, 46(3): 389 – 410.
[29] MANLIO B, TOMASO D C, GIOVANNI G, et al. TCP-based M2M traffic via random-access satellite links: throughput estimation. IEEE Trans. on Aerospace and Electronic Systems, 2018, 55(2): 846 – 863.
[30] NORBERG J, VIERINEN J, ROININEN L, et al. Gaussian Markov random field priors in ionospheric 3D multi-instrument tomography. IEEE Trans. on Geoscience and Remote Sensing, 2018, 56(12): 7009 – 7021.
[31] EKICI E, AKYILDIZ I F, BENDER M D. A distributed routing algorithm for datagram traffic in LEO satellite networks. IEEE/ACM Trans. on Networking, 2001, 9(2): 137 – 147.
[32] VAGHEFI R M, BUEHRER R M. Cooperative joint synchronization and localization in wireless sensor networks. IEEE Trans. on Signal Processing, 2015, 63(14): 3615 – 3627.
[33] XIONG Y F, WU N, SHEN Y, et al. Cooperative network synchronization: asymptotic analysis. IEEE Trans. on Signal Processing, 2018, 66(3): 757 – 772.
[34] ETZLINGER B, MEYER F, HLAWATSCH F, et al. Cooperative simultaneous localization and synchronization in mobile agent networks. IEEE Trans. on Signal Processing, 2017, 65(14): 3587 – 3602.
[35] YUAN W, WU N, ETZLINGER B, et al. Expectation – maximization-based passive localization relying on asynchronous receivers: centralized versus distributed implementations. IEEE Trans. on Communications, 2019, 67(1): 668 – 681.

Biographies

XU Xiaoyi was born in 1997. She received her B.E. degree from Shanghai University. She is a Ph.D. candidate of the Micro-Satellite Research Center, Zhejiang University. Her research interests include inter-satellite ranging, satellite network, and satellite constellation design.
E-mail: xiaoyixu@zju.edu.cn

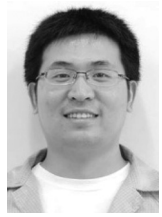

WANG Chunhui was born in 1983. He received his B.E. and Ph.D. degrees from Zhejiang University in 2004 and 2009 respectively. Now he is an associate professor of Zhejiang University. His research interests include analog transponder and high accuracy inter-satellite ranging system.
E-mail: hytgwch@zju.edu.cn

JIN Zhonghe was born in 1970. He received his Ph.D. degree from Zhejiang University in 1998. Now he is a professor of School of Aeronautics and Astronautics, Zhejiang University. His research interests include microsatellite and formation technology, micro-electro-mechanical systems (MEMS) and satellite measurement and control communication technology.
E-mail: jinzh@zju.edu.cn